Available online at www.sciencedirect.com

ScienceDirect

journal homepage: www.elsevier.com/locate/he

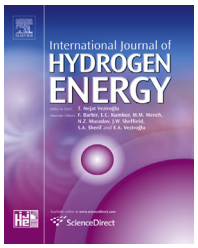

Evaluation of using protective/conductive coating on Fe-22Cr mesh as a composite cathode contact material for intermediate solid oxide fuel cells

Aroa Morán-Ruiz [a], *Karmele Vidal* [a], *Aitor Larrañaga* [a], *Jose Manuel Porras-Vázquez* [c], *Peter Raymond Slater* [c], *María Isabel Arriortua* [a,b,*]

[a] *Universidad del País Vasco (UPV/EHU), Facultad de Ciencia y Tecnología, Departamento de Mineralogía y Petrología, Barrio Sarriena S/N, 48940, Leioa, Vizcaya, Spain*

[b] *BCMaterials (Basque Centre for Materials, Applications & Nanostructures), Technological Park of Zamudio, Camino de Ibaizabal, Bndg. 500-1st, 48160, Derio, Spain*

[c] *University of Birmingham, School of Chemistry, Birmingham, B15 2TT, UK*

ARTICLE INFO

Article history:
Received 3 November 2014
Received in revised form
12 January 2015
Accepted 2 February 2015
Available online 7 March 2015

Keywords:
SOFC
Composite contact coating
Channeled interconnect
Chromium poisoning
Contact resistance

ABSTRACT

An uncoated and $MnCo_{1.9}Fe_{0.1}O_4$ (MCF) coated Fe-22Cr meshes were dipped into $LaNi_{0.6}Fe_{0.4}O_{3-\delta}$ (LNF) slurry to form a continuous protective/conductive layer for Crofer22APU interconnect. After aged these samples at 800 °C for 1000 h, energy dispersive X-ray (EDX) results concluded that: if the deposition of the protective coating was not enough to form a dense and continuous layer across the width of the mesh, then the use of MCF spinel layer is not enough to prevent chromium migration. For mesh-LNF/interconnect structure the area specific resistance (ASR) value of 0.0425(2) Ω cm^2 was stable for 400 min at 800 °C, indicating initial good adherence between both materials. After aged this structure at 800 °C for 1000 h, without applying a current source, X-ray micro-diffraction (XRMD) results, performed at the rib and channel of the interconnect, revealed that the LNF material is acting as a protective layer. Moreover, X-ray photoelectron spectroscopy (XPS) analysis indicated that manganese is concentrated on the mesh/LNF contact surface.

Introduction

Alternative technologies need to be developed for long-term sustainable energy supply due to socio-political, economic and environmental problems associated with the burning of fossil fuels. Solid oxide fuel cells (SOFCs) have the potential to be efficient and cost-effective system for the direct conversion of a wide variety of fuels to clean electricity. These benefits will only be achieved by society if SOFC technology can become commercially available [1,2].

Despite SOFC advantages, they still have problems related to: i) poor contact between cell component and ii)

* *Corresponding author*. Universidad del País Vasco (UPV/EHU), Facultad de Ciencia y Tecnología, Departamento de Mineralogía y Petrología, Barrio Sarriena S/N, 48940 Leioa, Vizcaya, Spain. Tel.: +34 946012534; fax: +34 946013500.
E-mail address: maribel.arriortua@ehu.es (M.I. Arriortua).
http://dx.doi.org/10.1016/j.ijhydene.2015.02.052

microstructure degradation of the porous electrodes due to chromium poisoning [3,4]. Growth of a poorly conductive oxide layer between the metallic interconnect ribs and the electrode results in a lack of contact between both materials. Moreover, the use of ferritic steel substrates is associated with another issue called "cathode Cr poisoning" [5]. Thus, the application of conductive/protective coatings acting as an adhesive to connect cathode with substrate, and as chromium diffusion barrier and oxide scale inhibitor is the subject of many research [6–8]. It is important to ensure that the materials exhibit high chemical and microstructural stability, high electrical conductivity, compatibility with the interconnect materials, reasonable thermal compatibility match with other cell components, and high sinterability to ensure high mechanical strength and good bonding with the adjacent components [9,10]. Various materials have been used in an effort to inhibit Cr migration from the chromia-rich subscales and to improve oxide scale-to-electrode adhesion, reducing oxide growth kinetics. Basically, SOFC interconnect coatings fall into four main categories [9]: reactive element oxides (REOs), MAlCrYO (M represents a metal, e.g., Co, Mn, Ti or Ni), conductive perovskites and spinels.

The perovskite structure oxides, $A^{3+}B^{3+}O^{2-}_{3-\delta}$, where A is a rare-earth element and B is a first row transition metal, have been investigated widely for cathode contact applications [11–13]. Compositions with B=Co, Ni have been used becouse of their high conductivity, while the oxides with B=Cr, Fe, Mn are known to be stable at high temperatures [1,14,15]. Moreover, the introduction of alkali-earth elements, such as Sr, increases the sintering activity and the conductivity [10,16]. Other authors indicated that $(La_{1-x}Sr_x)MnO_3$ coatings change the oxidation behavior and enhance the long term stability of metallic interconnects [17]. Moreover, more studies reported that [18] $La_{0.8}Sr_{0.2}CrO_3$ and $La_{0.8}Sr_{0.2}FeO_3$ coatings on ferritic alloys are not effective to prevent Cr outward diffusion. In another work, $(La,Sr)CoO_3$, $(La,Sr)(Co,Fe)O_3$ and $La(Ni,Fe)O_3$ coated ferritic alloys (Crofer22APU, E-Brite and 430) were studied [19], concluding that perovskite B-site cations (Ni,Fe,Co) diffuse to form stable spinel with transition metals from the interconnect. In our previous studies [20] $(La_{0.8}Sr_{0.2})_{0.95}Fe_{0.6}Mn_{0.3}Co_{0.1}O_3$, $LaNi_{0.6}Fe_{0.4}O_{3-\delta}$, $LaNi_{0.6}Co_{0.4}O_{3-\delta}$ were evaluated as contact materials between a Crofer22APU interconnect and a $La_{0.6}Sr_{0.4}FeO_3$ cathode. The formation of phases like $SrCrO_4$ and Cr-containing perovskite in short exposure times was observed. However, an adequate integrity and low reactivity is achieved when LNF contact coating is applied without compromising the contact resistance of the system.

Comparing to uncoated samples, perovskite coatings reduced the oxide scale growth so these coatings decrease the interfacial contact resistance; however, high sintering temperature of the perovskites leads to low compaction of these coatings and cell performance may still be degraded due to Cr poisoning. In addition to the perovskites, AB_2O_4 (A and B: divalent, trivalent and quadrivalent cations) spinel oxides can reduce oxidation and inhibit chromium volatility from ferritic stainless steels [9]. $Mn_{1-\delta}Co_{2-\delta}O_4$ spinels have been the most extensively studied [21–26]. However, ASR test of MCO coated Crofer22 showed that the adhesion of these coatings may be an issue for long-term applications [21,27]. For this reason Ce was added to the coating as reactive element in order to increase oxide scale and coating adherence to the metal substrate. A composition of $Ce_{0.05}Mn_{1.475}Co_{1.475}O_4$ was used and results have looked promising [28,29]. Moreover, other research groups have also studied Mn–Co spinels doped with Fe, Ti or Cu which exhibits higher electrical conductivity and a better densification than $MnCo_2O_4$ due to a partial substitution of Co by Fe, Ti and/or Cu [30–34]. Our previous work also concluded that [35] $MnCo_{1.9}Fe_{0.1}O_4$ was a more effective barrier than $MnCo_2O_4$, resulting in better electrochemical results and a similar microstructure; the presence of a low Fe content in $MnCo_{1.9}Fe_{0.1}O_4$ improved the stability of coating. In addition, due to the low cost of Ni, $NiMn_2O_4$ [36] and $NiFe_2O_4$ [37] spinels were also studied as protective coatings, providing effective conducting path to metallic substrate.

Despite the usefulness of conductive/protective coatings, the stack degradation rates are still higher than the required values for SOFC commercialization. It was found that $Ni_{80}Cr_{20}$/$(La_{0.75}Sr_{0.25})_{0.95}MnO_3$ dual-layer coating can improve the thermal stability and electrical performance of metallic interconnect [38]. In this context, according to other studies [39], the incorporation of conduction wires in the electrodes could increase cell performance via improved transport of electrons. In our previous work [40] a Fe–Cr mesh coated with $LaNi_{0.6}Co_{0.4}O_{3-\delta}$ high conductive perovskite was developed as an alternative to conventional contact materials. Taking into account that the generally accepted upper limit of ASR for SOFC interconnect is 0.1 Ω cm^2 [9,41,42], low and reproducible area specific resistance value (ASR) was achieved, being 0.0054(1) Ω cm^2, when this metallic/ceramic material was used to coat a channeled Crofer22APU interconnect.

In this study, LNF paste is developed to dip coated on Fe-22Cr mesh, forming a metallic/ceramic continuous layer in which ferritic mesh is fully covered with slurry. Because of Cr diffusion from steel was expected [40], the effectiveness of using MCF to protect mesh, prior to coat with LNF conductive perovskite, was discussed based on the long term behavior of these samples at 800 °C. LNF/MCF conductive/protective coatings were selected due to our previous experience and good results with these materials [20,35,43].

The obtained mixed material is expected to increase the conductivity and adhesive ability of the formed interface with interconnect ribs. Therefore, in order to evaluate this adherence, the resistance between these both materials was determined by relatively short-time ASR testing. Finally, this system was aged for 1000 h at 800 °C in order to establish the degradation trends under the rib (direct contact) and channel (no-contact) of the interconnect.

Experimental

The powder of $LaNi_{0.6}Fe_{0.4}O_{3-\delta}$ (LNF) was from fuel cell materials and, uncoated and $MnCo_{1.9}Fe_{0.1}O_4$ (MCF)-coated Fe-22Cr mesh (both with mesh opening of 175 μm and thickness of 250 μm) from Fiaxell SOFC Technologies (Crofer22H M_grid™ micro mesh). According to technical specifications the MCF coated mesh was sintered at 850 °C for 6 h, in air. LNF coating was applied onto uncoated and coated mesh squares (10 × 10 mm) by dipping them into the prepared ceramic

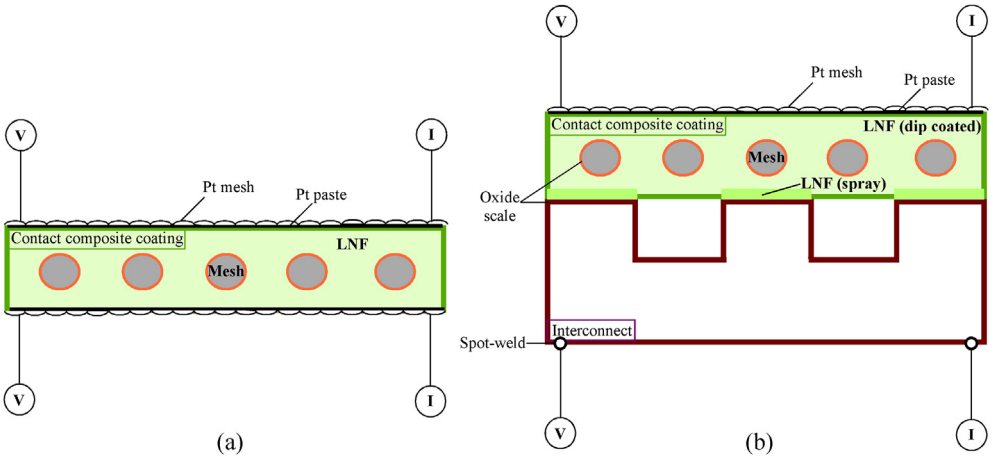

Fig. 1 – Schematic views of the used system configurations for ASR measurements: (a) composite contact material and (b) composite contact material on channeled interconnect.

slurry, thus obtaining a metallic/ceramic material. The LNF slurry was composed of ceramic powder (LNF, 12.5% in volume), dispersant (Dolapix, 1% relative to the ceramic powder, Zschimmer & Schwarz, Chemische Fabriken), binder (PVB, polyvinyl butyral, 5% relative to the ceramic powder, Solutia Solutions) and solvent (ethanol, 87.5% in volume, Panreac). The process performed to form a contact composite was described in Ref. [20]. The rheology of the suspensions was analyzed using a rheometer (HAAKE MARS II) at shear rates from 0.1 s^{-1} to 1000 s^{-1}, at room temperature. Composite materials were sintered at 1050 °C for 2 h and then treated at 800 °C for 1000 h, in air.

The composite contact material was directly bonded to a Crofer22APU channeled interconnect (ThyssenKrupp VDM). Nominal steel composition given by the supplier is summarized in Ref. [44]. The interconnect squares (10 × 10 × 1 mm) were preoxidized at 800 °C for 100 h, reducing Cr and Fe transport into the contact coating after long oxidation times [45]. The channel dimensions of the interconnect as well as the procedure to obtain {composite contact material/interconnect} system was detailed in previous work [40]. The obtained structure was sintered at 1050 °C for 2 h and then treated at 800 °C for 1000 h, in air.

X-ray diffraction (XRD) patterns of the samples were measured with an Philips X'Pert PRO diffractometer, powered at 40 kV and 40 mA using Cu K_α radiation (λ = 1.5418 Å) in air at room temperature. The patterns were recorded in 2θ steps of 0.026° in the 20–90° range, counting for 181 s for step. X-ray micro-diffraction (XRMD) data were collected using a Bruker D8 Discover diffractometer equipped with a Cr Twist tube, V filter (λ = 2.2898 Å), PolyCap™ (1μ single crystal cylinders) system for parallel been generation (divergence of 0.25°), and a 1-D LynxEye PSD detector (active length in 2θ 2.7°). The sample was mounted on an Eulerian Cradle with automatically controlled X-Y-Z stage. The sample illumination was adjusted with 1 mm PinHole collimator in the incident been, the position control was tested by using the interference of two lasers. Data were collected from 10 to 100° 2θ (step size = 0.04 and time per step = 10 s total time 6.5 h) at RT. Phases were identified from the measured XRD and XRMD patterns using X'Pert HighScore software based on the powder diffraction file (PDF) database. The fitting of a measured and calculated pattern was done by Rietveld method using the FULLPROF program [46].

X-ray photoelectron spectroscopy (XPS) measurements were performed using a XPS spectrometer (SPECS). All XPS

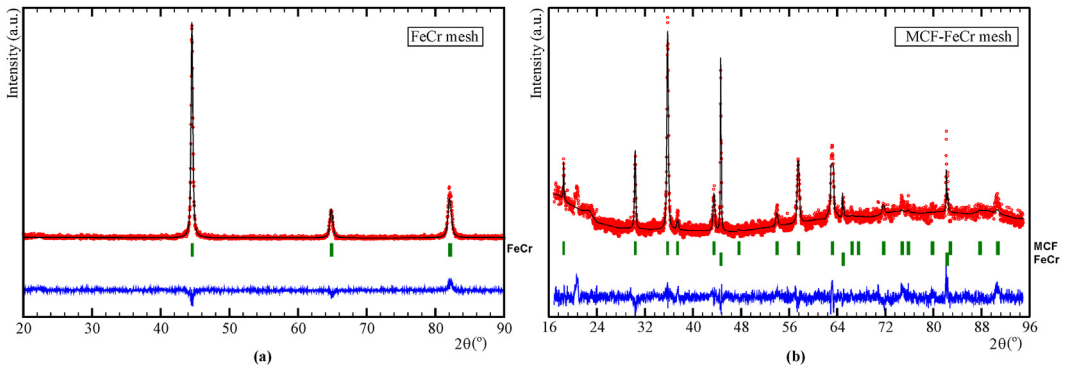

Fig. 2 – Rietveld X-ray diffraction patters for (a) commercial uncoated and (b) $MnCo_{1.9}Fe_{0.1}O_4$ spinel coated Fe-22Cr mesh.

Table 1 – Structural parameters for Fe-22Cr mesh and $MnCo_{1.9}Fe_{0.1}O_4$-coated Fe-22Cr mesh from the Rietveld refinement by using X-ray power diffraction data at room temperature.

Sample	Phase	Space group	Lattice parameters a (Å)	V (Å^3)	% in weight	χ^2
FeCr mesh	FeCr	*Im-3m*	2.876(1)	23.78(1)	100	5.42
MCF-FeCr mesh	MCF	*Fd-3m*	8.324(1)	576.78(1)	3.1(1)	1.70
	FeCr	*Im-3m*	2.871(1)	23.67(1)	96.9(8)	

spectra were acquired using a monochromatic X-ray source producing Al Kα radiation ($h \cdot \nu = 1486.6$ eV) and recorded using a SPECS PHOIBOS 150 analyzer. An initial analysis of the elements present in the sample was carried out (wide scan: step energy 1 eV, dwell time 0.1 s, pass energy 80 eV) and individual high resolution spectra were obtained (detail scan: step energy 0.1 eV, dwell time 0.1 s, pass energy 20 eV). The take-off angle of the photoelectrons was 90° with respect to the sample. The binding energies (BEs) were calibrated against the surface carbon contamination at 284.6 eV. The spectra were fitted by CasaXPS 2.3.16 software, modeling properly weighted sum of Gaussian and Lorentzian component curves, after background subtraction according to Shirley.

For microstructure and composition analysis, sample cross-sections were mounted in resin, polished and sputtered with coal graphite. A JEOL LSM-6400 instrument equipped with a tungsten filament gun and an Oxford Inca Pentafet X3 energy dispersive X-ray analyzer (EDX) was used to examine the samples. The operating voltage used was 20 kV and a current density of $1 \cdot 10^{-9}$ A. The EDX analysis was carried out through point analysis (the live time was set to 100 s).

Area Specific Resistance (ASR) measurements were performed using a DC four-probe method (the resistance value was estimated from the voltage value (Thurlby Thandar Instruments 1604 Digital Multimeter) measured on applying a current of 1A (Thurlby Thandar Instruments PL300 current source)), on both a composite and on a system, which were prepared according to the geometries shown in Fig. 1. Electrical contacts between samples and external measuring circuit were obtained by two Pt wires welded directly onto the sides of the interconnect and by Pt paste onto the surface of the composite contact material in combination with a Pt mesh.

Results and discussion

In order to investigate the crystal structure of uncoated and coated FeCr mesh squares, the samples were analyzed using X-ray diffraction (XRD) measurements (Fig. 2).

The refined cell parameters, unit cell volumes and the quality of the refinements are summarized in Table 1. For the coated mesh, MCF (3.1(1) % in weight) was quantified (Fig. 2b).

The phase structures of studied commercial $LaNi_{0.6}Fe_{0.4}O_{3-\delta}$ and Crofer22APU were analyzed in detail in our group [20]. The chemical composition of the surface of the alloys used as interconnect and, as mesh to form composite material were quantitatively analyzed using SEM-EDX. The measured values of the elements were checked on different points to obtain the average composition grade (Table 2). In order to ensure the determined chemical formulation of the samples, nominal compositions for each steel given by the technical specifications are also listed in Table 2.

As an example, Fig. 3 shows EDX spectra from one point results. The quantitative EDX analysis revealed that Fe–Cr mesh contains tungsten (W) and niobium (Nb), in contrast to interconnect which did not present these elements.

The strength of a steel is related to the combination of solid solution and precipitation strengthening given by Nb and W addition [47]. Lanthanum, titanium and niobium additives are concentrated in specific regions of the alloy (identified as A point of each sample in Fig. 4) differently from tungsten, which is dissolved in the ferritic matrix. Thus, the average chemical composition of steels showed undetectable levels of La and low concentrations for Ti and Nb for EDX technique.

The characterization of LNF slurry rheology is important for coated thickness control during the dip coating process. The effort against the shear rate of LNF paste is represented graphically in Fig. 5. As shown, the slurry behaves like a Newtonian fluid, and so the viscosity values are independent of the shear rate.

The viscosity value can be extracted from the slope of the represented line, being 0.038 Pa s, in good agreement with obtained results in our previous studies [40].

Effectiveness of using a protective coating on Fe–Cr mesh

The formed Fe–Cr mesh/LNF and Fe–Cr mesh/MCF/LNF composites, after sintering at 1050 °C for 2 h in air, are shown

Table 2 – Chemical composition in wt (%) of Fe-22Cr alloy used as interconnect and as mesh, given by the technical specifications and obtained by EDX microanalysis.

Sample		Fe (%wt.)	Cr (%wt.)	Mn (%wt.)	Ti (%wt.)	Nb (%wt.)	W (% wt.)	Si (%wt.)	Al (%wt.)	Cu (%wt.)	La (%wt.)
Crofer22H	Min.	Bal.[a]	20.0	0.3	0.02	0.2	1.0	0.1			0.04
	Max.		24.0	0.8	0.20	1.0	3.0	0.6	0.1	0.5	0.20
Mesh	EDX	73.1(3)	23.5(2)	0.6(1)	<0.1	0.4(1)	2.3(2)	–	–	–	–
Crofer22APU	Min.	Bal.[a]	20.0	0.3	0.03	–	–				0.04
	Max.		24.0	0.8	0.20	–	–	0.50	0.50	0.50	0.20
Interconnect	EDX	76.3(2)	23.0(2)	0.6(1)	<0.1	–	–	–	–	–	–

[a] Balance.

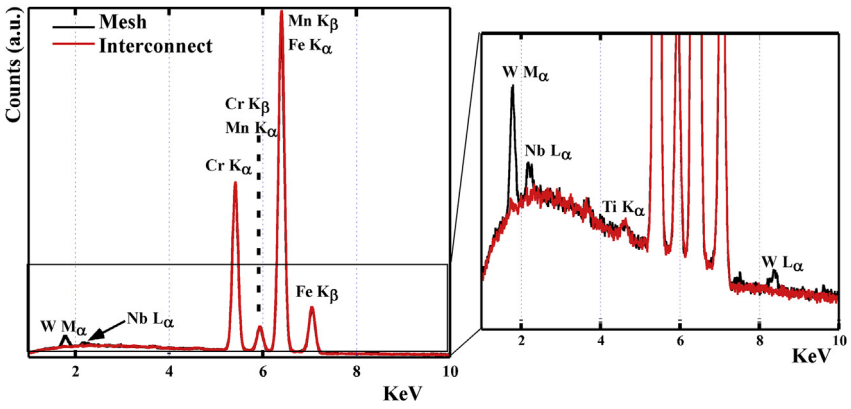

Fig. 3 – EDX spectra analyses for Fe-22Cr interconnect and mesh samples.

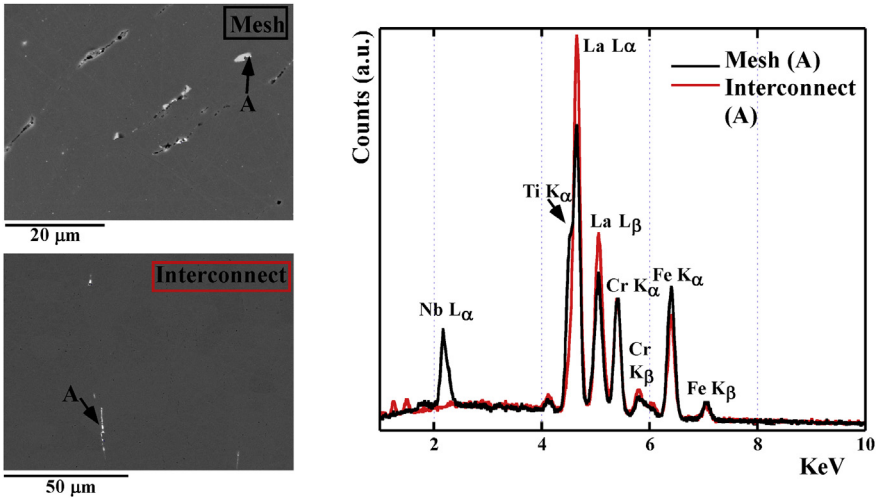

Fig. 4 – EDX point analysis performed on specific regions of the alloys.

in Fig. 6. As observed from Fig. 6a, the ceramic coating is continuous and homogeneous along the samples. However, the MCF protective coating was not a continuous layer along the width of the Fe–Cr mesh (Fig. 6b). Laves phase precipitates were observed along the steel grain boundaries [48], in good agreement with Fig. 6.

The area specific resistance (ASR) values of sintered Fe–Cr/LNF and Fe–Cr/MCF/LNF composite materials were 0.00453(1) and 0.00341(1) Ω cm^2, respectively. Despite the observed porous coarse microstructure in both LNC and MCF coatings (Fig. 6), the determined low ohmic resistance confirms that the use of these composite materials as a contact layer is adequate.

EDX point analysis was performed on a cross-section of just sintering at 1050 °C for 2 h mesh/LNF material (Fig. 7), and compared with another sample after heat treated at 800 °C for 1000 h in air (Fig. 8).

The obtained k ratios for identified elements, in these both samples, were listed in Table 3 (corresponding to Fig. 7) and Table 4 (corresponding to Fig. 8).

Moreover, Fig. 9 and Table 5 show a cross-section microstructure image of $MnCo_{1.9}Fe_{0.1}O_4$ coated mesh after dipping

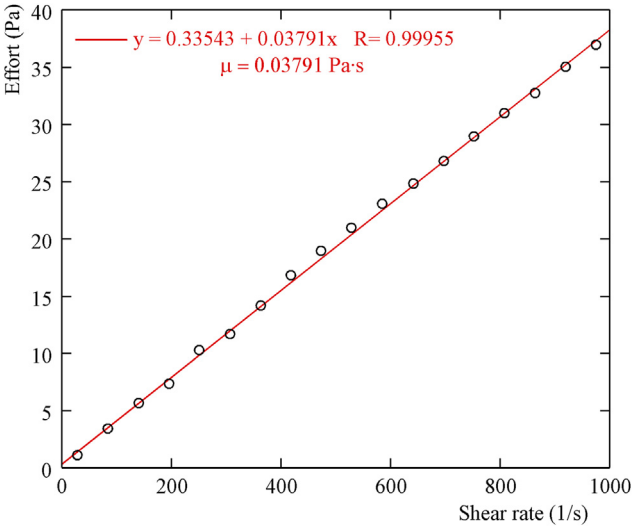

Fig. 5 – Plot of the effort against shear rate of $LaNi_{0.6}Fe_{0.4}O_{3-\delta}$ paste.

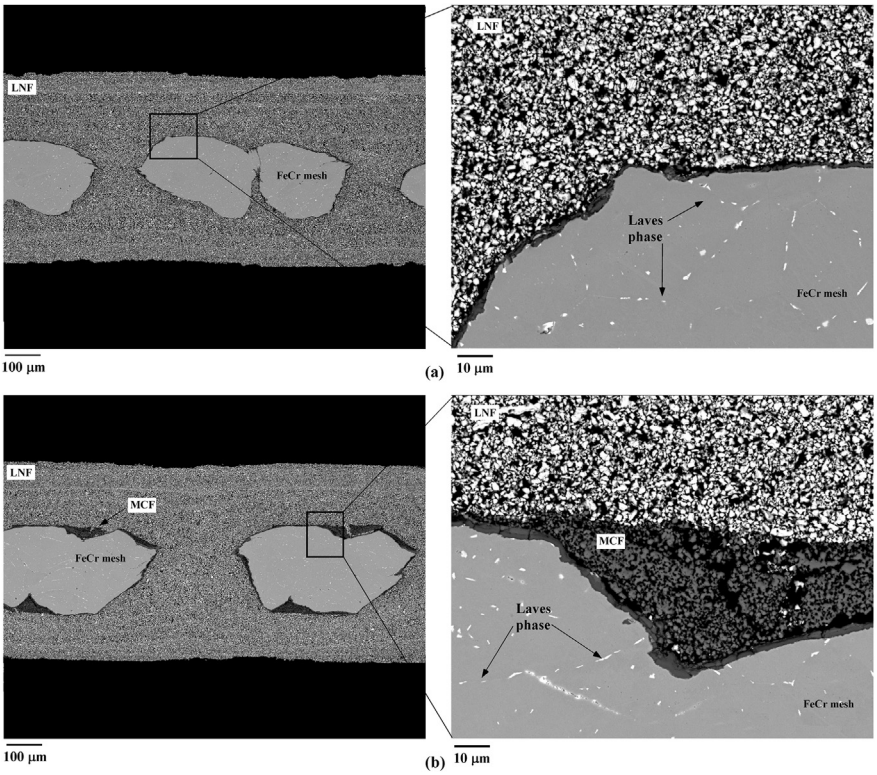

Fig. 6 – SEM cross-section of (a) Fe-22Cr mesh and (b) MCF coated Fe-22Cr mesh after dipping into LNF slurry and the following sintering at 1050 °C for 2 h, in air.

into $LaNi_{0.6}Fe_{0.4}O_{3-\delta}$ slurry with EDX point analysis, and the obtained elemental k ratios, respectively. The INCA 350 software from Oxford was used to reconstruct the spectra, separating the overlapping peaks.

The ceramic/metallic interface was relatively smooth in the initial composite (Fig. 7), while the interface was more irregular in the LNF dip coated mesh after 1000 h at 800 °C (Fig. 8), as was expected [49]. Moreover, locally internal precipitates, which could be related to the external not uniform oxide scale [50], were also found. According to microstructure, LNF showed relatively inhomogeneity between sintered particles, which could decrease their adherence to the alloy [51,52]. Thus, these particle contact points are irregular through the mesh surface that might also be associated to the observed irregular oxide scale, being noticeable after 1000 h at 800 °C. Therefore, for both Fe–Cr mesh/LNF materials ceramic layer contains pores whereas some of them are formed at the scale interface. Thus, especially the long-term heat treated sample shows areas without contact. As observed from Fig. 9, for spinel coated mesh loss of adherence was observed between the $MnCo_{1.9}Fe_{0.1}O_4$ protective and LNF contact layers. According to Ref. [30] the formation of these cracks could be as

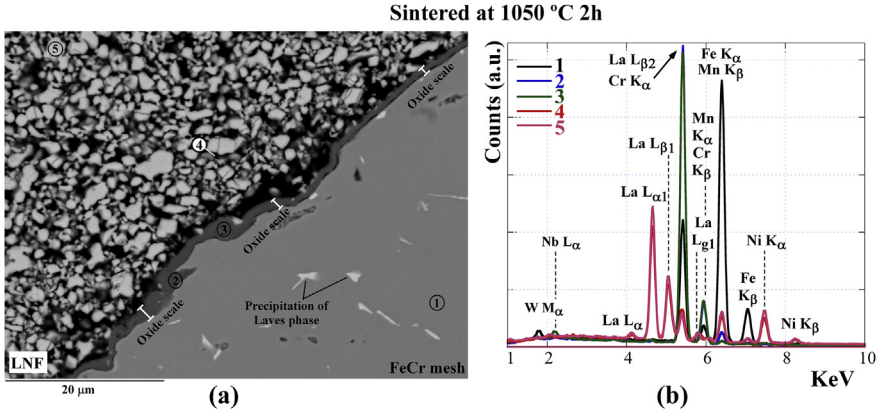

Fig. 7 – (a) Cross-section microstructure image obtained by backscattered electrons signal (BSE) and (b) EDX analysis on different points of LNF/mesh sintered at 1050 °C for 2 h, in air.

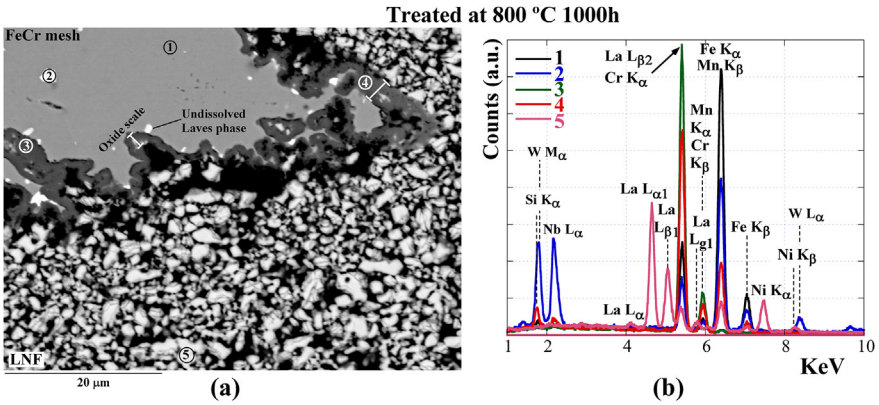

Fig. 8 – (a) Cross-section microstructure (BSE) and (b) EDX analysis on different points of LNF/mesh sintered at 1050 °C and then treated at 800 °C for 1000 h, in air.

Table 3 – Elemental k ratios measured by EDX point analysis performed on mesh/LNF just sintering at 1050 °C for 2 h, in air (corresponding to Fig. 7).

Spectrum	Cr (k ratio)	Fe (k ratio)	Mn (k ratio)	La (k ratio)	Ni (k ratio)	Nb (k ratio)	W (k ratio)
1	0.24	0.65	–	–	–	–	0.01
2	0.58	0.03	–	–	–	–	–
3	0.57	0.01	0.01	0.01	0.01	0.01	–
4	0.03	0.06	–	0.43	0.1	–	–
5	–	0.08	–	0.50	0.13	–	–

Table 4 – K ratios for identified elements on mesh/LNF sample after sintered and aged at 800 °C for 1000 h, in air (corresponding to Fig. 8).

Spectrum	Cr (k ratio)	Fe (k ratio)	Mn (k ratio)	La (k ratio)	Ni (k ratio)	Nb (k ratio)	W (k ratio)	Si (k ratio)
1	0.19	0.74	–	–	–	–	0.01	–
2	0.09	0.41	–	–	–	0.12	0.18	–
3	0.61	0.01	0.01	–	–	0.01	–	–
4	0.45	0.19	–	0.01	–	0.01	–	0.01
5	–	0.08	–	0.52	0.13	–	–	–

a result of cooling down to room temperature. However, MCF spinel layer showed different microstructures between points 3, 4 and 5 (Fig. 9), which could be related to the protective layer thickness, being in the zone where point 3, 4 were analyzed higher than in the point 5 analyzed area. In this way, the highest thickness allowed high enough density to improve adherence between metallic substrate and protective coating. The EDX point analysis, which were made on alloy, revealed in

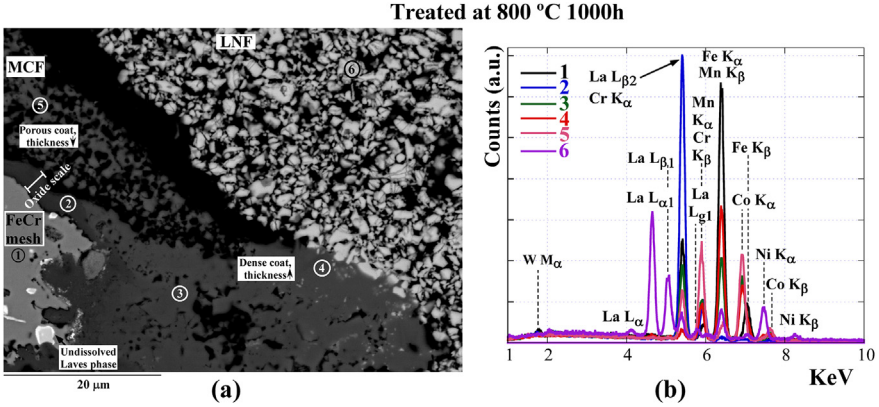

Fig. 9 – (a) Cross-section BSE image and (b) EDX point analysis of MCF coated mesh after dipping into LNF paste and the following sintering and aging processes.

Table 5 – The corresponding k ratios for identified elements on mesh/MCF/LNF sample after sintered and heat treated at 800 °C for 1000 h, in air (corresponding to Fig. 9).

Spectrum	Cr (k ratio)	Fe (k ratio)	Mn (k ratio)	La (k ratio)	Ni (k ratio)	Co (k ratio)	W (k ratio)
1	0.19	0.65	0.01	–	–	–	0.01
2	0.56	0.01	0.01	–	–	–	–
3	0.15	0.2	0.07	–	–	0.19	–
4	0.02	0.33	0.07	0.01	0.02	0.17	–
5	0.09	0.02	0.19	–	0.01	0.28	–
6	–	0.07	–	0.47	0.13	–	–

most of the cases α-Fe(Cr,W) phase. The analysed Laves phase precipitates (Fig. 8, point 2) were composed of $(Fe,Cr)_2(Nb,W)$, in good agreement with Ref. [48], in which Laves phase precipitates of Fe_2Nb type were formed on small additions of Nb. The combined additions of Nb and Si, which came from the alloy, allowed the formation of Fe–Cr–Nb–Si system [53], as can observed in Fig. 8, point 4. However, the results showed that the Nb was also incorporated in the external oxide scale. In some areas of Figs. 8 and 9, there is undissolved Laves phase in contact with the scale, indicating the thermodynamic stability of this compound.

According to EDX analysis, for sample without MCF protective layer, a passive chromia layer (Cr_2O_3/$(Mn,Cr)_3O_4$ [35]) about 1.3 μm thick (measured directly from Fig. 8) was grown between the metal substrate and the LNF coating. For the spinel coated mesh specimen, an oxide scale was also formed beneath the MCF coating, in good agreement with EDX analysis. According to our previous studies [44], the presence of Fe in oxide scale indicated the formation of small amount of hematite phase (α-Fe_2O_3) and/or Fe_3O_4 phases. Moreover, the appearance, in the oxide scale, of Cr, Mn and Fe simultaneously allows the formation of $(Mn,Fe,Cr)_3O_4$ spinel. In addition, EDX point analyses, performed on the interface close to the contact coating, indicated the migration of lanthanum and nickel from the LNF layer into the passive oxide scale or MCF protective layer. However, due to the porosity of the sample, and because the resolution of the energy dispersive X-rays source from the sample is approximately 1 μm, it is noted that the point analysis results should be interpreted with caution.

With EDX, evidence of Cr penetration through the protective spinel coating, as well as into the LNF coating, was found. Darker grey-colored Cr-rich grains were observed in the LNF coating for uncoated and coated FeCr mesh samples, which decrease as the distance from the mesh is increased (Figs. 8 and 9). In terms of the microstructure, the open porosity observed in LNF and MCF coatings might reduce the adherence to the alloy and enhance the transport of Cr to gas phase.

Since the deposition of the commercial protective coating was not homogeneous across the width of the Fe-22Cr mesh, the use of an MCF spinel protective layer is not enough to prevent chromium migration up to the contact coating. Thus, the uncoated sample was selected to evaluate the electrical performances of the composite contact material/interconnect system, including long-term contact stability of the metallic/ceramic composite material under the rib (direct contact) and channel (no-contact) of the interconnect.

Characterization of the composite contact material with channeled Crofer22APU interconnect

Ceramic/metallic material was directly adhered to the channeled substrate and sintered at 1050 °C for 2 h. Results from ASR test (Fig. 10) showed initial good stability of the signal during the contact resistance measurements, and thus a good adherence between both materials, exhibiting ASR value of 0.0425(2) Ω cm^2 for 400 min, in air.

Fig. 11 shows a representative SEM cross-section of the post-test composite-coated Crofer22APU interconnect on which EDX point analyses were performed. When comparing different EDX spectra, similar compositions were observed. All of the analyzed particles are composed mainly of La, Ni, Fe, and amounts of Cr. However, Fig. 10b shows the lowest chromium content distribution in point 1.

The results of the initial characterization indicate that the developed coated interconnect system shows a low area specific resistance value since the generally accepted upper limit of ASR for SOFC substrate is 0.1 Ω cm^2 [9,41,42]. Its contact resistance is also smaller than those reported in other studies [13,54,55], in which the electrical performance of perovskite coated metallic interconnect was studied. Thus, the mesh/LNF layer could be a suitable alternative for the SOFC interconnect coatings development.

Long-term stability of the system

The sintered system composed of {LNF-steel mesh contact composite/Crofer22APU channeled interconnect} was treated at 800 °C for 1000 h, in air. Fig. 12 shows X-ray micro-

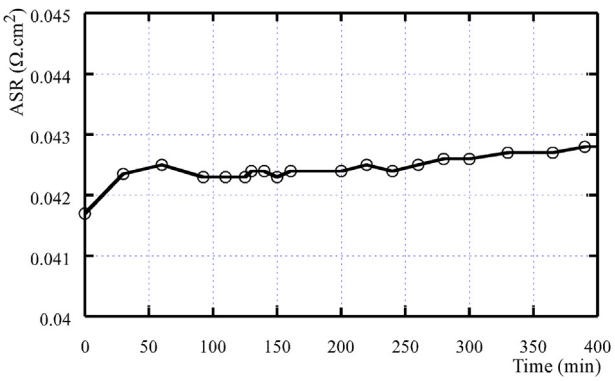

Fig. 10 – ASR for {composite contact material/channeled interconnect} interface as a function of time.

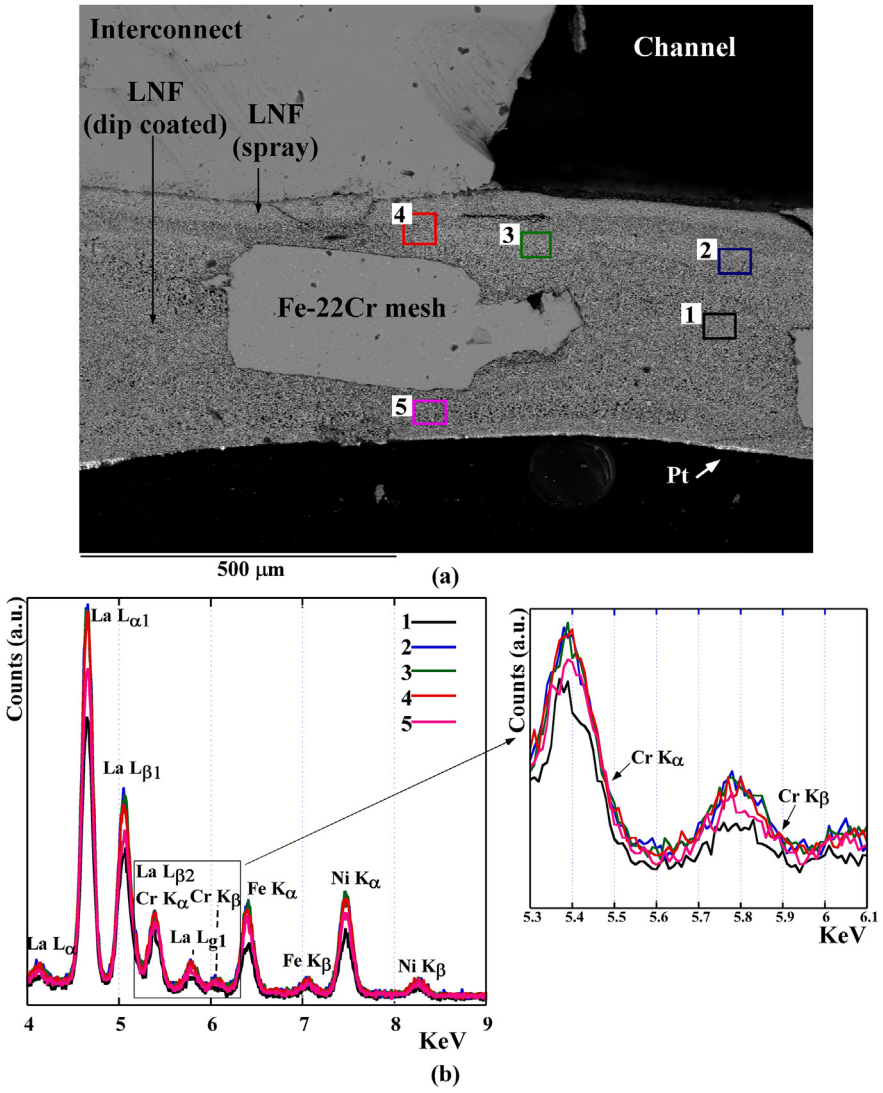

Fig. 11 – (a) SEM cross-section of studied system after ASR test with corresponding (b) EDX point analysis.

diffraction pattern refinements performed on the rib (Fig. 12a) and the channel (Fig. 12b) of the interconnect in contact with the composite material, after the long term treatment.

The formed phases and their quantitative analysis (% in weight) are presented in Table 6. These analyses reveal that in the rib zone the main and secondary phases were $LaNi_{0.6}Fe_{0.4}O_3$ (83.4(8)% in weight) and $La(Ni,Fe,Cr)O_3$ (13.3(4)% in

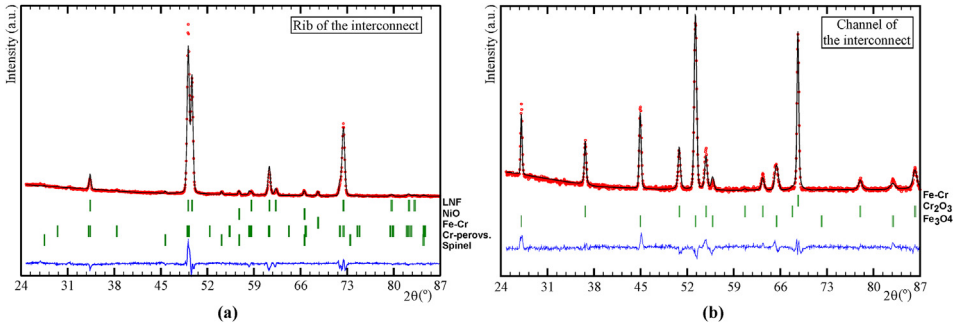

Fig. 12 – X-ray micro-diffraction pattern refinements performed (a) on the rib and (b) on channel of the interconnect in contact with composite material, after long term heat treatment.

Table 6 – X-ray micro-diffraction quantitative (%wt.) analysis of the formed phases on the rib and channel of the interconnect in contact with composite material after long-term heating in air.

Phase	Space group	N° PDF	Rib (%wt.)	Channel (%wt.)
$LaNi_{0.6}Fe_{0.4}O_3$	R-3c	88-0637	83.2(8)	–
$La(Ni,Fe,Cr)O_3$	Pbnm	24-1016	13.3(4)	
Fe–Cr	Im3m	34-0396	1.1(1)	16.2(2)
NiO	Fm-3m	73-1519	2.2(2)	–
$MnCr_2O_4$	Fd-3m	31-0630	<0.2	–
Cr_2O_3	R-3c	85-0730	–	13.9(3)
Fe_3O_4	Fd-3m	19-0629	–	69.9(8)

weight) as well as, NiO, Fe–Cr, and $(Cr,B)_3O_4$ spinel (B = Fe, Mn, Ni), respectively. In contrast, the channel zone results show as the main phase Fe_3O_4 (69.9(8)% in weight) and as secondary phases: Fe–Cr, and Cr_2O_3.

The original Fe–Cr substrate was identified indicating that the X-ray penetration was enough to observe the signal of all the formed layers. The presence of NiO might entail that Ni is partially extracted from the LNF perovskite lattice, allowing the formation of $La(Ni,Fe,Cr)O_3$, in good agreement with Ref. [56].

The LNF ceramic coating might act as a protective coating. Hence, Cr_2O_3 and Fe_3O_4 phases are observed on the channels. Furthermore, the absence of Cr_2O_3 on the rib of the interconnect, can also imply that chromium has completely reacted to form Cr-perovskite and/or $(Cr,B)_3O_4$ (B= Mn, Fe, Ni) spinel phase. An interconnect without ceramic coating at long exposure to air, can promote Fe_3O_4 formation rather than the formation of a chromia/spinel protective scale, concluding in the formation of a non-protective or Fe-rich scale [57–60].

Fig. 13 shows the surface of the composite material which was in contact with the interconnect, after long term IT-SOFC conditions, EDX point analysis is also shown. The corresponding k ratios for identified elements in each point were listed in Table 7.

Two different areas were identified at the composite contact surface: the area of the composite i) under the rib and ii) under channel of the interconnect. In both zones, the qualitative EDX analyses indicate that the analyzed grains contain La, Ni, Fe and Cr elements. Thus, the composite direct contacted (the rib) and no-contacted (channel) with the interconnect present similar elements distribution. These results indicate that the dominant cause for system degradation depends on both Cr vaporization from the interconnect steel and solid phase diffusion of Cr from the mesh alloy [61].

Table 7 – Elemental k ratios measured by EDX point analysis performed on mesh/LNF material which was in contact with the interconnect after 1000 h at 800 °C, in air (corresponding to Fig. 13).

Spectrum	La (k ratio)	Ni (k ratio)	Fe (k ratio)	Cr (k ratio)
1	0.4	0.11	0.06	0.02
2	0.34	0.1	0.05	0.02
3	0.46	0.12	0.07	0.03
4	0.31	0.08	0.04	0.02
5	0.45	0.12	0.07	0.03

The composite contact surface was also characterized using XPS. Five relatively strong peaks were detected in the observed channel and rib contact areas of the surface of the metallic/ceramic composite material, after long-term heat treatment, using wide scan to 1385 eV, attributable to O 1s, Cr 2p, Mn 2p, Fe 2p and La 3d photoelectrons in Fig. 14.

The deconvolution of these peaks for both studied zones is shown in Fig. 15 (surface of the composite under channel) and Fig. 16 (surface of the composite under the rib).

Detailed analysis of the main deconvolution peaks, including binding energies (BEs) and relative atomic percentage concentration of detected elements are listed in Table 8.

The data measured in the present study were compared with the XPS spectra for perovskite-type oxide structures [62,63]. This comparison indicated, in both areas, for La, there are two peaks, one at ~833 eV corresponding to La^{3+} in perovskite phase and, another at ~835 eV which is assigned to La^{3+} in La_2O_3, in good agreement with our previous studies [20]. In addition, the binding energies of ~710 eV and ~712 eV could allow the presence of iron in perovskite [64]. Thus, the

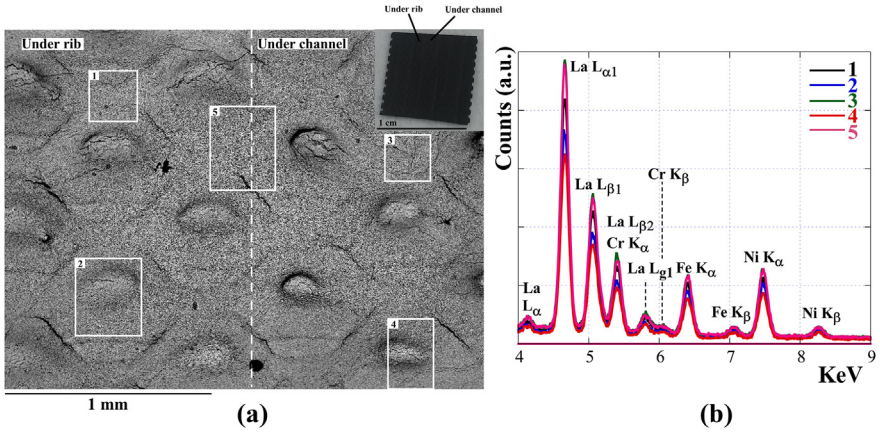

Fig. 13 – (a) SEM image and (b) EDX point analysis of the surface of the composite material which was in contact with the interconnect, after heated at 800 °C for 1000 h, in air.

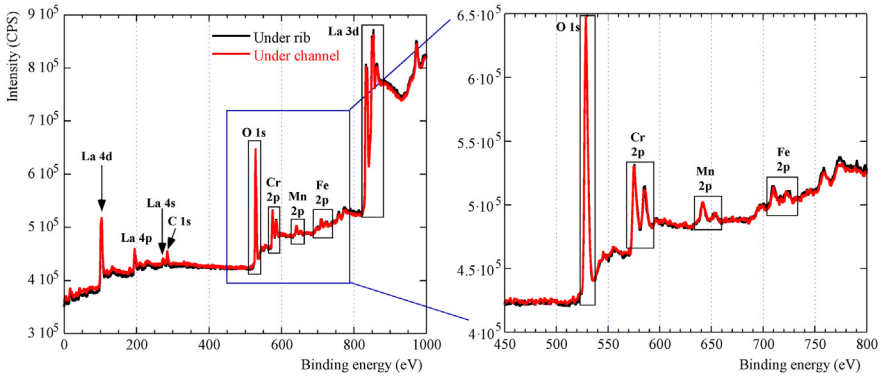

Fig. 14 – Wide scan XPS spectra of composite contact material under the rib and channel after long-term heated at 800 °C in air.

peaks appearing at ~575 eV, ~576 eV and ~579 eV indicated the appearance of chromium in perovskite with ABO_3 structure [40,65] (Table 8), in good agreement with the obtained XRMD results in which Cr-perovskite was quantified (Table 6). Besides, in Ref. [56], the $LaNi_{0.6}Fe_{0.4}O_3$ stability in the presence of chromia was investigated, concluding Cr-cations moves into the perovskite structure, replacing first Ni- and then Fe-cations. The presence of nickel was not detected by XPS, which could indicate the exchange of Ni with Cr in the initial perovskite structure. In addition, for both analyzed zones, the presence of Mn is observed from the peaks at ≈642 eV, ≈644 eV and ≈647 eV (Mn $2p_{3/2}$), in good agreement with other authors [66–68].

Analyses from both EDX and XPS showed similar results for the analyzed composite material areas which were in contact with interconnect. According to other authors [69], the XPS technique is more sensitive for surface composition analysis and detects a depth of ~5 nm while EDX is able to measure ~1 μm depth. Thus, the difference means that Mn is more concentrated on the composite surface (surface in contact with the rib and under channel of the interconnect), not through the bulk, providing the formation of a low thickness

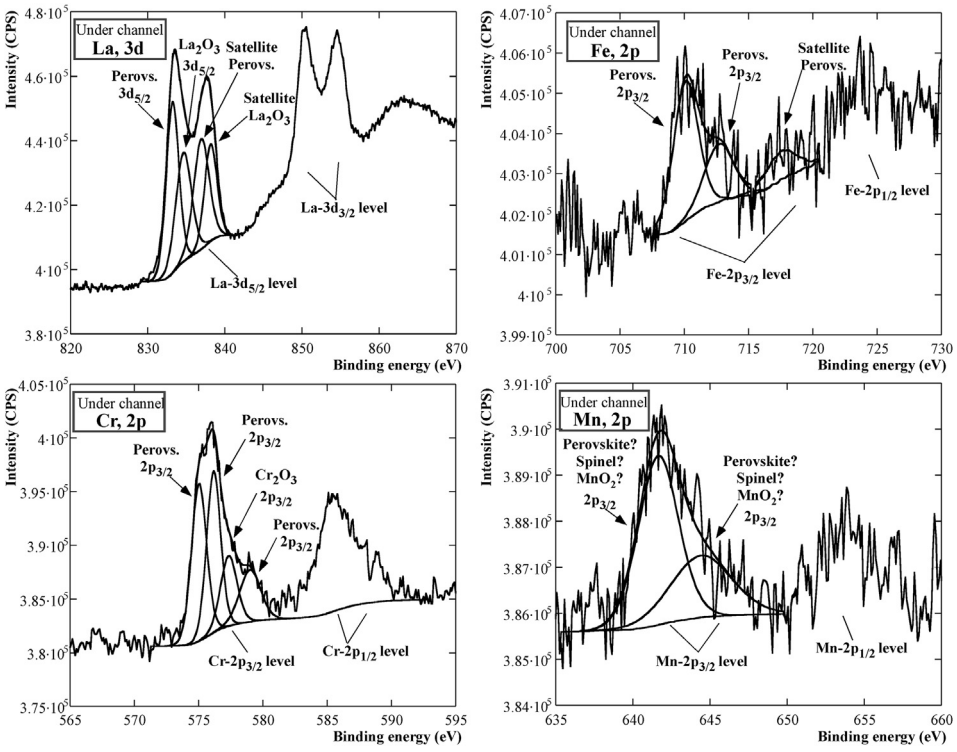

Fig. 15 – Detailed XPS spectra of La $3d_{5/2}$, Cr $2p_{3/2}$, Mn $2p_{3/2}$ and Fe $2p_{3/2}$ of the surface of LNF/Fe-22Cr composite contact material under the channel of the interconnect, after long-term heated at 800 °C in air.

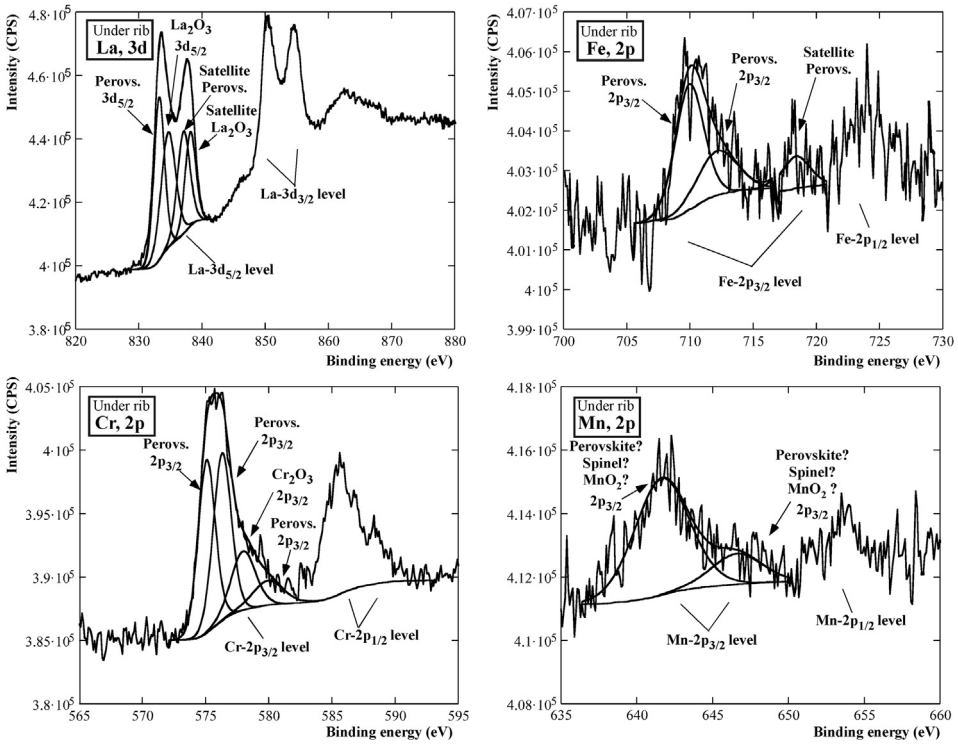

Fig. 16 – Deconvolution of La $3d_{5/2}$, Cr $2p_{3/2}$, Mn $2p_{3/2}$ and Fe $2p_{3/2}$ XPS peaks identified on the surface of LNF/Fe-22Cr composite contact material under the rib of the interconnect, after long-term heated at 800 °C in air.

Mn-spinel barrier layer [70]. This might also partly explain why the detected (% in weight) $MnCr_2O_4$, by XRMD, is low.

Evaluation of the long-term chemical compatibility of the studied system revealed that the direct exposure to air increased the oxidation of interconnect, leading to the growth of a Cr_2O_3 layer and formation of Fe_3O_4 oxide on the channel of the alloy substrate. Since chromium appears to have a tendency to incorporate into the LNF structure, this material could be considered a suitable candidate for reducing the degradation of the cell.

Conclusions

An uncoated and $MnCo_{1.9}Fe_{0.1}O_4$ (MCF) coated Fe-22Cr meshes were dipped into $LaNi_{0.6}Fe_{0.4}O_{3-\delta}$ (LNF) slurry to form a continuous conductive/protective layer for Crofer22APU interconnect. It has been demonstrated that if the deposition of the protective coating was not enough to form a dense and continuous layer across the width of the Fe-22Cr mesh, then the use of MCF spinel layer is not enough to prevent chromium migration up to the LNF coating. However, when mesh/LNF material was directly adhered to the interconnect, the obtained ASR value of 0.0425(2) Ω cm^2 was stable for 400 min, indicating initial good adherence between both materials. The evaluation of long-term chemical compatibility of this system, without applying a current source, revealed that the presence of a composite coating on the rib of interconnect limited the growth of the chromia-based layer and formation of iron oxides on alloy substrate, reducing the contact resistance of the system. Future work will include electrochemical measurements of mesh-LNF/interconnect structure for extended periods.

Table 8 – XPS analysis results of detected elements for the contact surface of the composite in contact with the rib and under channel of the interconnect, after heating at 800 °C for 1000 h in air.

Peak	Surface under channel		Surface in contact with the rib	
	BE (eV)	% at. conc.	BE (eV)	% at. conc.
La $3d_{5/2}$ in ABO_3	833.22; 836.95 (sat.)	9.2	833.23; 837.09 (sat.)	8.8
La $3d_{5/2}$ in La_2O_3	834.65; 838.16 (sat.)	7.0	834.66; 838.17 (sat.)	7.9
Cr $2p_{3/2}$ in ABO_3	575.04; 576.17; 579	8.3	575.1; 576.32; 579.94	8.4
Cr $2p_{3/2}$ in Cr_2O_3	577.35	1.7	577.99	1.8
Fe $2p_{3/2}$ in ABO_3	710.1; 712.69; 717.53 (sat.)	1.7	709.96; 712.17; 718.38 (sat.)	1.8
Mn $2p_{3/2}$	641.65; 644.42	2.6	641.65; 646.59	2.8
O 1s	528.85; 530.46; 531.72; 532.9	69.5	528.89; 530.57; 531.76; 533.26	68.5

Acknowledgements

This research has been funded by the Dpto. Educación, Política Lingüística y Cultura of the Basque Goverment (Research Group of the Basque University System IT-630-13), Ministerio de Economía y Competitividad (MAT2013-42092-R) and Engineering and Physical Sciences Research Council (EP/I003932). The authors wish to thank SGIker-UPV/EHU technical and human support. Dr. Mª Belén Sánchez Martínez de Ilárduya is acknowledged for useful scientific help in discussion of XPS measurements. The authors would also like to express their gratitude to Dr. Sergio Fernandez Armas for helping with EDX measurements. A. Morán-Ruiz thanks UPV/EHU for funding her PhD work.

REFERENCES

[1] Millar L, Taherparvar H, Filkin N, Slater P, Yeomans J. Interaction of $(La_{1-x}Sr_x)_{1-y}MnO_3$-$Zr_{1-z}Y_zO_{2-\delta}$ cathodes and $LaNi_{0.6}Fe_{0.4}O_3$ current collecting layers for solid oxide fuel cell application. In: Proceedings of the 2008 conference for the engineering doctorate in environmental technology.

[2] Sharaf OZ, Orhan MF. An overview of fuel cell technology: fundamentals and applications. Renew Sust Energy Rev 2014;32:810–53.

[3] Guan W, Jin L, Wu W, Zheng Y, Wang G,Wang WG. Effect and mechanism of Cr deposition in cathode current collecting layer on cell performance inside stack for planar oxide fuel cells. J Power Sources 2014;245:119–28.

[4] Guan WB, Jin L, Ma X, Wang WG. Investigation of impactors on cell degradation inside planar SOFC stacks. Fuel Cells 2012;6:1085–94.

[5] Schuler JA, Wuillemin Z, Hessler-Wyser A, Comminges C, Steiner NY, Van Herle J. Cr-poisoning in $(Ls,Sr)(Co,Fe)O_3$ cathodes after 10.000 h SOFC stack testing. J Power Sources 2012;211:177–83.

[6] Tucker MC, Cheng L, DeJonghe LC. Selection of cathode contact materials for solid oxide fuel cells. J Power Sources 2011;196:8313–22.

[7] Guan WB, Zhai HJ, Jin L, Li TS, Wang WG. Effect of contact between electrode and interconnect on performance of SOFC stacks. Fuel Cells 2011;3:445–50.

[8] Stodolny MK, Boukamp BA, Blank DHA, Van Berkel FPF. Cr-poisoning of $LaNi_{0.6}Fe_{0.4}O_3$ cathode under current load. J Power Sources 2012;209:120–9.

[9] Shaigan N, Qu W, Douglas GI, Chen W. A review of recent progress in coatings, fuel cell ferritic stainless steel interconnects. J Power Sources 2010;195:1529–42.

[10] Lu Z, Xia G, Templeton JD, Li X, Nie Z, Yang Z, et al. Development of $Ni_{1-x}Co_xO$ as the cathode/interconnect contact for solid oxide fuel cells. Electrochem Commun 2011;13:642–5.

[11] Tietz F, Sebold D. Interface reactions between electrically conductive ceramics and ferritic steel-I. The system Cr-22Fe-0.5Mn/Mn_2O_3/(La,Ca)(Cr,Co,Cu)O_3. Mater Sci Eng B 2008;150:135–40.

[12] Sharma VI, Yildiz B. Degradation mechanism in $La_{0.8}Sr_{0.2}CoO_3$ as contact layer on the solid oxide electrolysis cell anode. J Electrochem Soc 2010;157(3):B441–8.

[13] Montero X, Tietz F, Stöver D, Cassir M, Villarreal I. Comparative study of perovskites as cathode contact materials between an $La_{0.8}Sr_{0.2}FeO_3$ cathode and a Crofer22APU interconnect in solid oxide fuel cells. J Power Sources 2009;188:148–55.

[14] Basu RN, Tietz F, Teller O, Wessel E, Buchkremer HP, Stöver D. $LaNi_{0.6}Fe_{0.4}O_3$ as a cathode contact material for solid oxide fuel cells. J Solid State Electrochem 2003;7:416–20.

[15] Konysheva E, Laatsch J, Wessel E, Tietz F, Christiansen N, Singheiser L, et al. Influence of different perovskite interlayers on the electrical conductivity between $La_{0.65}Sr_{0.3}MnO_3$ and Fe/Cr based steels. Solid State Ionics 2006;177:923–30.

[16] Zhou Q, Xu L, Guo Y, Jia D, Li Y, Wei WCJ. $La_{0.6}Sr_{0.4}Fe_{0.8}Cu_{0.2}O_{3-\delta}$ perovskite oxide as cathode for IT-SOFC. Int J Hydrogen Energy 2012;37(16):11963–8.

[17] Da Conceiçao L, Dessemond L, Djurado E, Souza MMVM. $La_{0.7}Sr_{0.3}MnO_3$-coated SS444 alloy by dip-coating process for metallic interconnect supported solid oxide fuel cells. J Power Sources 2013;241:159–67.

[18] Yang Z, Xia GG, Maupin GD, Stevenson JW. Evaluation of perovskite overlay coatings on ferritic steels for SOFC interconnect applications. J Electrochem Soc 2006;153:A1852–8.

[19] Lacey R, Pramanick A, Lee JC, Jung JI, Jiang B, Edwards DD, et al. Evaluation of Co and perovskite Cr-blocking thin films on SOFC interconnects. Solid State Ionics 2010;181:1294–302.

[20] Morán-Ruiz A, Vidal K, Laguna-Bercero MA, Larrañaga A, Arriortua MI. Effects of using $(La_{0.8}Sr_{0.2})_{0.95}Fe_{0.6}Mn_{0.3}Co_{0.1}O_3$ (LSFMC), $LaNi_{0.6}Fe_{0.4}O_{3-\delta}$ (LNF) and $LaNi_{0.6}Co_{0.4}O_{3-\delta}$ (LNC) as contact material on solid oxide fuel cells. J Power Sources 2014;248:1067–76.

[21] Magdefrau NJ. Evaluation of solid oxide fuel cell interconnect coatings: reaction layer microstructure, chemistry and formation mechanisms [Doctoral dissertations]. University of Connecticut; 2013.

[22] Fang Y, Wu C, Duan X, Wang S, Chen Y. High-temperature oxidation process analysis of $MnCo_2O_4$ coatings on Fe-21Cr alloy. Int J Hydrogen Energy 2011;36(9):5611–6.

[23] Abdoli H, Alizadeh. Electrophoretic deposition of $(Mn,Co)_3O_4$ spinel nano poder on SOFC metallic interconnects. Mater Lett 2012;80:53–5.

[24] Uehara T, Yasuda N, Okamoto M, Baba Y. Effect of Mn-Co spinel coating for Fe-Cr ferritic alloys ZMG232L and 232J3 for solid oxide fuel cell interconnects on oxidation behavior and Cr-evaporation. J Power Sources 2011;196(17):7251–6.

[25] Zhang HH, Zeng CL. Preparation and performances of Co-Mn spinel coating on a ferritic stainless steel interconnect material for solid oxide fuel cell application. J Power Sources 2014;252:122–9.

[26] Zhang H, Wu J, Liu X, Baker A. Studies on elements diffusion of Mn/Co coated ferritic stainless steel for solid oxide fuel cell interconnects application. Int J Hydrogen Energy 2013;38:5075–83.

[27] Akanda SR, Walter ME, Kidner NJ, Seabaugh MM. Lifetime prediction for manganese cobalt spinel oxide coatings on metallic interconnects. Thin Solid Films 2014;565:237–48.

[28] Yang Z, Xia G, Nie Z, Templeton JD, Stevenson JW. Ce-modified $(Mn,Co)_3O_4$ spinel coatings on ferritic stainless steels for SOFC interconnect applications. Electrochem Solid St 2008;11(8):B140–3.

[29] Chou YS, Stevenson JW, Choi JP. Long-term evaluation of solid oxide fuel cell candidate materials in a 3-cell generic stack test fixture, part III: stability and microstructure of Ce-(Mn,Co)-spinel coating, AISI441 interconnect, alumina coating, cathode and anode. J Power Sources 2014;257:444–53.

[30] Montero X, Jordán N, Pirón-Abellán J, Tietz F, Stöver D, Cassir M, et al. Spinel and perovskite protection layers between Crofer22APU and $La_{0.8}Sr_{0.2}FeO_3$ cathode materials

for SOFC interconnects. J Electrochem Soc 2009;156(1):B188–96.
[31] Chou PY, Ciou CJ, Lee YC, Hung IM. Effect of $La_{0.1}Sr_{0.9}Co_{0.5}Mn_{0.5}O_{3-\delta}$ protective coating layer on the performance of $La_{0.6}Sr_{0.4}Co_{0.8}Fe_{0.2}O_{3-\delta}$ solid oxide fuel cell cathode. J Power Sources 2012;197:12–9.
[32] Hosseini N, Abbasi MH, Karimzadeh F, Choi GM. Development of $Cu_{1.3}Mn_{1.7}O_4$ spinel coating on ferritic stainless steel for solid oxide fuel cell interconnects. J Power Sources 2015;273:1073–83.
[33] Puranen J, Pihlatie M, Lagerbom J, Bolelli G, Laakso J, Hyvärinen L, et al. Post-mortem evaluation of oxidized atmospheric plasma sprayed Mn-Co-Fe oxide spinel coatings on SOFC interconnects. Int J Hydrogen Energy 2014;39(30):17284–94.
[34] Montero X, Tietz F, Sebold D, Buchkremer HP, Ringuede A, Cassir M, et al. $MnCo_{1.9}Fe_{0.1}O_4$ spinel protection layer on commercial ferritic steels for interconnect applications in solid oxide fuel cells. J Power Sources 2008;184:172–9.
[35] Miguel-Pérez V, Martínez-Amesti A, Nó ML, Larrañaga A, Arriortua MI. The effect of doping $(Mn,B)_3O_4$ materials as protective layers in different metallic interconnects for solid oxide fuel cells. J Power Sources 2013;243:419–30.
[36] Zhang W, Pu J, Chi B, Jian L. $NiMn_2O_4$ spinel as an alternative coating material for metallic interconnects of intermediate temperature solid oxide fuel cells. J Power Sources 2011;196:5591–4.
[37] Liu Y, Chen DY. Protective coatings for Cr_2O_3-forming interconnects of solid oxide fuel cells. Int J Hydrogen Energy 2009;34:9220–6.
[38] Wu W, Guan W, Wang G, Liu W, Zhang Q, Chen T, et al. Evaluation of $Ni_{80}Cr_{20}/(La_{0.75}Sr_{0.25})_{0.95}MnO_3$ dual layer coating on SUS 430 stainless steel used as metallic interconnect for solid oxide fuel cells. Int J Hydrogen Energy 2014;39:996–1004.
[39] Yoon C. Computational design, fabrication, and characterization of microarchitectured solid oxide fuel cells with improved energy efficiency [Ph D thesis]. Georgia Institute of Technology; 2010.
[40] Morán-Ruiz A, Vidal K, Larrañaga A, Laguna-Bercero MA, Porras-Vázquez JM, Slater PR, et al. $LaNi_{0.6}Co_{0.4}O_{3-\delta}$ dip-coated on Fe-Cr mesh as a composite cathode contact material on intermediate solid oxide fuel cells. J Power Sources 2014;269:509–19.
[41] Zhu WZ, Deevi SC. Development of interconnect materials for solid oxide fuel cells. Mat Sci Eng A-Struct 2003;348:227–43.
[42] Piccardo P, Gannon P, Chevalier S, Viviani M, Burbucci A, Caboche G, et al. ASR evaluation of different kinds of coatings on a ferritic stainless steel as SOFC interconnect. Surf Coat Tech 2007;202:1221–5.
[43] Vidal K, Morán-Ruiz A, Larrañaga A, Porras-Vázquez JM, Slater PR, Arriortua MI. Characterization of $LaNi_{0.6}Fe_{0.4}O_3$ perovskite synthesized by glycine-nitrate combustion method. Solid State Ionics 2015;269:24–9.
[44] Miguel-Pérez V, Martínez-Amesti A, Nó ML, Larrañaga A, Arriortua MI. Oxide scale formation on different metallic interconnects for solid oxide fuel cells. Corros Sci 2012;60:38–49.
[45] Hoyt KO, Gannon PE, White P, Tortop R, Ellingwood BJ, Khoshuei H. Oxidation behavior of $(Co,Mn)_3O_4$ coatings on preoxidized stainless steel for solid oxide fuel cell interconnects. Int J Hydrogen Energy 2012;37:518–29.
[46] Rodríguez-Carvajal J. FULLPROF rietveld pattern matching analysis of powder patterns. 2011 [Grenoble].
[47] Froitzheim J, Meier GH, Niewolak L, Ennis PJ, Hattendorf H, Singheiser L, et al. Development of high strength ferritic steel for interconnect application in SOFCs. J Power Sources 2008;178:163–73.
[48] Chiu YT, Lin CK. Effects of Nb and W additions on high-temperature creep properties of ferritic stainless steels for solid oxide fuel cell interconnect. J Power Sources 2012;198:149–57.
[49] Linder M, Hocker T, Holzer L, Friedrich KA, Iwanschitz B, Mai A, et al. Cr_2O_3 scale growth rates on metallic interconnectors derived from 40.000 h solid oxide fuel cell stack operation. J Power Sources 2013;243:508–18.
[50] Ali-Löytty H. Microalloying mediated segregation and interfacial oxidation of FeCr alloys for solid oxide fuel cell applications [Ph. D. thesis]. Tampere University of Technology; 2013.
[51] Mohammadi M, Javadpoura S, Kobayashi A, Shirvani K, Jenabali JA, Khakpour I. Cyclic oxidation behavior of CoNiCrAlY coatings produced by LVPS and HVOF processes. Trans JWRI 2011;40:53–8.
[52] Fayette S, Smith DS, Smith A, Martin C. Influence of grain size on the thermal conductivity of tin oxide ceramics. J Eur Ceram Soc 2000;20(3):297–302.
[53] Vilasi M, Francois M, Brequel H, Podor R, Venturini G, Steinmetz J. Phase equilibria in the Nb-Fe-Cr-Si system. J Alloy Compd 1998;269:187–92.
[54] Ming-Jui T, Chun-Lin C, Shyong L. $La_{0.6}Sr_{0.4}Co_{0.2}Fe_{0.8}O_3$ protective coatings for solid oxide fuel cell interconnect deposited by screen printing. J Alloy Compd 2010;489:576–81.
[55] Tucker MC, Cheng L, DeJonghe LC. Inorganic binder-containing composite cathode contact materials for solid oxide fuel cells. J Power Sources 2013;224:174–9.
[56] Stodolny MK, Boukamp BA, Blank DHA, Van Berkel FPF. $La(Ni,Fe)O_3$ stability in the presence of chromia-A solid-state reactivity study. J Electrochem Soc 2011;158(2):B112–6.
[57] Wang K, Liu Y, Fergus JW. Interaction between SOFC interconnect coating materials and chromia. J Am Ceram Soc 2011;94(12):4490–5.
[58] Shong WJ, Liu CK, Chen CY, Peng CC, Tu HJ, Fey GTK, et al. Effects of lanthanum-based perovskite coatings on the formation of oxide scale for ferritic SOFC interconnect. Mater Chem Phys 2011;127:45–50.
[59] Stojanovic M, Haverkamp RG, Mims CA, Moudallal H, Jacobson AJ. Synthesis and characterization of $LaCr_{1-x}Ni_xO_3$ perovskite oxide catalysts. J Catal 1997;165:315–23.
[60] Essuman E, Meier GH, Zurek J, Hänsel M, Norby T, Singheiser L, et al. Protective and non-protective scale formation of NiCr alloys in water vapour containing high- and low-pO_2 gases. Corros Sci 2008;50(6):1753–60.
[61] Jiang SP, Chen X. Chromium deposition and poisoning of cathodes of solid oxide fuel cells-A review. Int J Hydrogen Energy 2014;39(1):505–31.
[62] Crumlin EJ, Mutoro E, Liu Z, Grass ME, Biegalski MD, Lee YL, et al. Surface strontium enrichment on highly active perovskites for oxygen electrocatalysis in solid oxide fuel cells. Energy Environ Sci 2012;5:6081–8.
[63] Konysheva EY, Francis SM. Identification of surface composition and chemical states in composites comprised of phases with fluorite and perovskite structures by X-ray photoelectron spectroscopy. Appl Surf Sci 2013;268:278–87.
[64] Ghaffari M, Shannon M, Hui H, Tan OK, Irannejad A. Preparation, surface state and band structure studies of $SrTi_{(1-x)}Fe_{(x)}O_{(3-\delta)}$ (X = 0-1) perovskite-type nano structure by X-ray and ultraviolet photoelectron spectroscopy. Surf Sci 2012;606:670–7.
[65] Jiang Y, Gao J, Liu M, Wang Y, Meng G. Synthesis of $LaCrO_3$ films using spray pyrolysis technique. Mater Lett 2007;61:1908–11.
[66] Nesbitt HW, Banerjee D. Interpretation of XPS Mn(2p) spectra of Mn oxyhydroxides and constraints on the mechanism of MnO_2 precipitation. Am Mineral 1998;83:305–15.

[67] Ramana CV, Massot M, Julien CM. XPS and Raman spectroscopic characterization of $LiMn_2O_4$ spinels. Surf Interface Anal 2005;37:412–6.
[68] Wei ZX, Xiao CM, Zeng WW, Liu JP. Magnetic properties and photocatalytic activity of $La_{0.8}Ba_{0.2}Fe_{0.9}Mn_{0.1}O_{3-\delta}$ and $LaFe_{0.9}Mn_{0.1}O_{3-\delta}$. J Mol Catal A-Chem 2013;370:35–43.
[69] Li W, Lu K, Xia Z. Interaction of $(La_{1-x}Sr_x)_nCo_{1-y}Fe_yO_{3-\delta}$ cathodes and AISI 441 interconnect for solid oxide fuel cells. J Power Sources 2013;237:119–27.
[70] Sabioni ACS, Huntz AM, Borges LC, Jomard F. First study of manganese diffusion in Cr_2O_3, polycrystals and thin films, by SIMS. Phil Mag Lett 2007;87(12):1921–37.